Author Manuscript

Accepted for publication in a peer-reviewed journal

NIST National Institute of Standards and Technology • U.S. Department of Commerce

Published in final edited form as:

Carbon N Y. 2019 ; 142: . doi:10.1016/j.carbon.2018.10.085.

Gateless and reversible carrier density tunability in epitaxial graphene devices functionalized with chromium tricarbonyl

Albert F. Rigosi[†,*], **Mattias Kruskopf**[†,‡], **Heather M. Hill**[†], **Hanbyul Jin**[†,‡], **Bi-Yi Wu**[†,£], **Philip E. Johnson**[†], **Siyuan Zhang**[†,⊥], **Michael Berilla**[†], **Angela R. Hight Walker**[†], **Christina A. Hacker**[†], **David B. Newell**[†], and **Randolph E. Elmquist**[†]

[†]National Institute of Standards and Technology (NIST), Gaithersburg, MD 20899, USA

[‡]Joint Quantum Institute, University of Maryland, College Park, MD 20742, USA

[£]Graduate Institute of Applied Physics, National Taiwan University, Taipei 10617, Taiwan

[⊥]Theiss Research, La Jolla, CA 92037, United States

Abstract

Monolayer epitaxial graphene (EG) has been shown to have clearly superior properties for the development of quantized Hall resistance (QHR) standards. One major difficulty with QHR devices based on EG is that their electrical properties drift slowly over time if the device is stored in air due to adsorption of atmospheric molecular dopants. The crucial parameter for device stability is the charge carrier density, which helps determine the magnetic flux density required for precise QHR measurements. This work presents one solution to this problem of instability in air by functionalizing the surface of EG devices with chromium tricarbonyl -$Cr(CO)_3$. Observations of carrier density stability in air over the course of one year are reported, as well as the ability to tune the carrier density by annealing the devices. For low temperature annealing, the presence of $Cr(CO)_3$ stabilizes the electrical properties and allows for the reversible tuning of the carrier density in millimeter-scale graphene devices close to the Dirac point. Precision measurements in the quantum Hall regime show no detrimental effect on the carrier mobility.

Graphical Abstract

[*]Corresponding author. albert.rigosi@nist.gov;.

Author Contributions

A.F.R and M.K. have contributed equally to this manuscript. A.F.R., M.K. and R.E.E. developed the experimental design and the EG functionalization process. A.F.R., M.K., H.J., B.-Y.W., and P.E.J. performed transport measurements. M.B. assisted with assembling electronics for the QHR measurement system. H.M.H. performed Raman measurements and analysis. S.Z. and C.A.H. performed XPS measurements and analysis. M.K. and R.E.E. produced graphene samples. A.R.H.W., R.E.E., and D.B.N provided general project support and guidance. The manuscript was written through contributions of all authors. All authors have given approval to the final version of the manuscript.

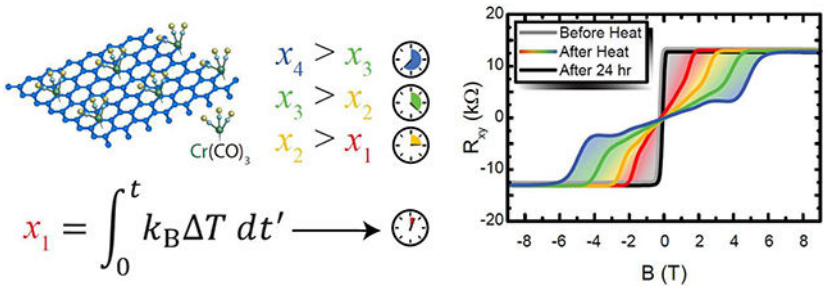

1. INTRODUCTION

Due to its advantageous electrical properties, graphene has been the subject of extensive study over more than a decade.[1–3] Among the variety of ways developed to synthesize graphene, epitaxial graphene (EG) on silicon carbide (SiC) displays superior properties for the development of quantized Hall resistance (QHR) standards.[4–11] Developing highly efficient standards using EG requires the long-term stability of electrical properties of millimeter-scale EG devices in ambient conditions, to equal the long-term stability and precision of GaAs-AlGaAs heterostructure QHR devices.[11] These properties include the longitudinal conductivity σ_{xx}, carrier density n, and mobility μ, which are related by the equation $\sigma_{xx} = ne\mu$.

While initial efforts to realize millimeter-scale EG devices for metrology have been fruitful, electrostatic gating for devices of this size and application is quite difficult. One early and successful process used to reduce the carrier density for QHR devices was photochemical gating, using ZEP-520A electron beam positive tone resist as an electron acceptor, but the process reversibility has inherent limitations based on number of thermal cycles to which a device is exposed.[12] Other methods for carrier density control and conservation have also been explored,[13–14] such as the use of poly-methyl methacrylate (PMMA),[12,15] atomically layered dielectrics,[16–19] Parylene,[20–21] amorphous boron nitride,[22–23] and hexagonal boron nitride.[24–25], but were either unable to achieve metrological usefulness,[20,22] or are irreversible processes.[15]

When EG is exposed to ambient atmospheric conditions, it experiences a drift in the carrier density and conductivity because of the physisorption of H_2O and O_2, which are found to be p-doping species because of their oxidizing characteristic.[26–29] Achieving electrical stability is critical for device applications including mass-produced electronics, chemical and biological sensors, and functionalized materials. This motivation holds particularly true for resistance metrology, where a narrow range of carrier densities between 1×10^{11} cm^{-2} and 3×10^{11} cm^{-2} is needed to produce a resistance plateau of $R_{xy} = \frac{e^2}{2h}$ at easily accessible magnetic flux densities (B). Generally, lower carrier densities will yield unreliable plateaus and higher carrier densities correlate to a plateau onset at higher magnetic flux densities.[11] Thus, gateless control of the carrier density is crucial to improving accessibility of resistance metrology using EG, where this $\nu = 2$ plateau can exhibit precise quantization at low magnetic fields (between 2.5 T and 7 T) for carrier densities in the vicinity of 10^{11} cm^{-2}.[4]

In this work, we report the gateless and reversible carrier density tunability in EG devices functionalized with chromium tricarbonyl [$Cr(CO)_3$]. We have observed carrier density stability in air over the course of one year with shifts less than 10^{11} cm^{-2}, and by controllable and reversible tuning, achieved metrologically useful values of the QHR, rendering $Cr(CO)_3$ as a suitable compound for stabilizing electrical devices based on EG. Controllable tuning was demonstrated by annealing the device in vacuum to the desired carrier density while monitoring the device's room-temperature longitudinal resistivity. Despite exposure to heating in vacuum at up to 363 K (90 °C), EG devices retained full functionalization, and when stored in air for typically 24 h to 36 h following the anneal and measurement, the device's carrier density drifted back to a low value, on the order of 10^{10} cm^{-2}, with respect to inherent EG doping above 10^{13} cm^{-2}. These results demonstrated that this functionalization method can be used to stabilize and reversibly tune the carrier density in millimeter-scale EG devices without the need of electrostatic gating, reducing the level of processing required for useful devices. Furthermore, these devices exhibited properties suitable for resistance metrology with proper tuning.

2. SAMPLE PREPARATION

2.1 EG Growth and Device Fabrication

EG is formed during thermal decomposition of the SiC substrate causing an enrichment of the surface with carbon atoms due to the preferential sublimation of silicon atoms. Samples used for this study were grown using 4H-SiC(0001) semi-insulating substrates with a miscut of ≤ 0.10°. Before growth, the substrates were first cleaned by piranha etch, followed by a dip into diluted hydrofluoric acid and a surface treatment with polymer adsorbates for polymer-assisted sublimation growth (PASG) by spin coating a weak solution (approximately 2 $ml_{[AZ5214E]}$ / $l_{[isopropanol]}$).[30] For graphene growth, the resulting SiC(0001) samples were placed on a polished disk of glassy carbon with the Si face in direct contact with the disk for face-to-graphite growth.[8] Combining the PASG and face-to-graphite growth methods suppresses the formation of etch pits and high substrate steps as well as related bilayer domains. The annealing process at 1900 °C was performed in argon at atmospheric pressure with a graphite-lined resistive-element furnace. After growth, EG was inspected with confocal laser scanning and optical microscopy to rapidly identify successful growths over large areas.[31]

2.2 EG Functionalization with $Cr(CO)_3$

The concept of functionalizing EG with $Cr(CO)_3$ was motivated, in part, by pursuits to alter the electronic structure of graphene without drastically modifying the in-plane transport properties, and to date, several groups use different forms of graphene to study the mechanisms behind hexahapto functionalization.[32–37] Covalent functionalization by this method does not fully passivate the EG surface, but greatly reduces the level of electron doping in EG devices and helps to limit the long-term drift in carrier density levels. For our method, which follows closely that of Ref. 35, the completed EG device was placed in a phosphor-bronze (Ph-Br) boat and loaded into a small homemade vacuum furnace shown in Figure 1 (a). The chamber was then purged with nitrogen gas and heated slightly above 130 °C for 2 h while keeping the load lock slightly open to remove any lingering adsorbates

on the surface of the EG device. After placing approximately 100 mg of crystalline $Cr(CO)_6$ (chromium hexacarbonyl) in a separate section of the Ph-Br sample boat, the system was closed, and nitrogen flow was stopped. The furnace temperature was then raised to 130 °C, using the optimized conditions set forth by Ref. 36. The $Cr(CO)_6$ sublimates and reacts with the surface of EG, resulting in the ring-centered $Cr(CO)_3$ functionalization. An illustration of this mechanism is provided in Figure 1 (a), as well as an optical image of one of the devices in Figure 1 (b). The sample space was then evacuated using a liquid nitrogen cold trap for about 30 minutes before the chamber was cooled down and opened. Out of seven fabricated devices used in this study, six were functionalized using the vacuum furnace method.

3. SAMPLE CHARACTERIZATION

3.1 Raman Spectroscopy

Raman spectroscopy was utilized to monitor the behavior of the 2D (G') peak of the EG before and after the functionalization process. Spectra were collected with a Renishaw InVia micro-Raman spectrometer[see notes] using a 633 nm wavelength excitation laser source and a backscattering configuration. The spot size was about 1 μm, the acquisition times were 300 s, the laser power was 1.7 mW power, and the optical path included a 50 × objective and 1200 mm^{-1} grating. Rectangular Raman maps were collected with step sizes of 20 μm in a 5 by 3 raster-style grid. The presence of $Cr(CO)_3$ on the EG surface yielded a modified 2D (G') peak with a smaller intensity, redshifted position, and larger width. The average changes in intensity, position, and width for the case before and after functionalization corresponded to a factor of 0.68 ± 0.05, a redshift of 4 cm^{-1} ± 0.5 cm^{-1}, and a broadening of 51.3 cm^{-1} ± 10.5 cm^{-1}, as shown in Figure 1 (c) using two examples (all uncertainties represent 1σ deviations). The effects have been observed with other amorphous materials deposited on EG.[22] Only the 2D (G') peak was used to assess the changes of the EG surface due to the overwhelmingly large SiC response in the G peak region.

3.2 X-Ray Photoelectron Spectroscopy

X-ray photoelectron spectroscopy (XPS) measurements on functionalized EG devices were performed in a commercial instrument equipped with a monochromatic Al Kα excitation photon source and a hemispherical electron analyzer. All XPS measurements were performed at a base pressure of 2.7×10^{-7} Pa or less, electron take-off angle of 0° with respect to the surface normal, and an energy resolution of 0.1 eV. The spectra in Figure 1 (d) show the fittings done for the spectral regions relevant to C 1s in the top panel and Cr 2p in the bottom panel. For binding energies near the carbon region, EG and SiC show contributions of carbon around 283 eV, C-O at 285 eV, and C=O at 287 eV. Analyzing the Cr 2p peaks required the fitting to include chromium oxide compounds. The Cr $2p_{3/2}$ peak can be deconvoluted into two peaks at binding energies of 576 eV and 577 eV, assigned to graphene bonded $Cr(CO)_3$ and CrO_3, respectively. Though the observed components of the functionalization process are expected and reported in the literature, their relative intensities were much higher compared to adjacent atoms like carbon.[32–34,36,38–39] This observation is explained and resolved in the Supplementary Data.

4. RESULTS AND DISCUSSION

4.1 Gateless and Reversible Tuning of the Carrier Density

Six functionalized devices and one control device were tested for carrier density stability. By annealing the device at a fixed temperature for a prolonged time in vacuum and within the cryogenic measuring system, ranging from 5 min to 90 min, the carrier density becomes more *n*-type. The integrated heat exposure (IHE) is a figure of merit used to quantify the applied changes to the device caused by annealing:

$$IHE = \int_0^t k_B\left(T_{\text{applied}} - T_{RT}\right)dt' \quad (1)$$

T_{RT} is taken to be 300 K, k_B is the Boltzmann constant, and the integral is evaluated over time in seconds. Repeatable annealing was achieved using proportional–integral–derivative (PID) controllers that require some time to reach temperatures as high as 360 K, and so the effects of annealing between room temperature and the desired temperature must be accounted for. While annealing, only the longitudinal resistivity, a quantity that is correlated with the carrier density, was monitored. At room temperature while in vacuum or inert gases such as helium, the longitudinal resistivity shifted by less than 100 Ω overnight, compared to the typical value of up to 10 kΩ, (see Supplementary Data), making it a negligible shift compared with that above room temperature. After annealing, the carrier density and mobility were derived from cryogenic transport measurements in a 9 T superconducting magnet system.

To evaluate a device's carrier density, one can use the relation $n_e = \frac{1}{e\left(\frac{dR_{xy}}{dB}\right)}$, where n_e is the carrier density, e is the elementary charge, B is the magnetic flux density, and R_{xy} is the Hall resistance, using SI units for all quantities. As shown in the gray curves in Figure 2 (a), before the device was annealed, the Hall resistance data indicated low carrier densities, on the order of 10^{10} cm^{-2}. The carrier density increased as a consequence of annealing at a temperature between 300 K and 360 K for varying periods of time, resulting in an IHE (or x_i as shown abstractly in each panel) on the order of 10^{-18} J·s. The device was able to retain this carrier density in vacuum or helium at 300 K, before its exposure to air. Once the device was in air, the carrier density returned to its low value as before within roughly 24 hr. During this process, the longitudinal resistivity was monitored with time, and is plotted in Figure 2 (b). Two exponential decay terms were used to describe the device's asymptotic approach to 15.5 kΩ for reasons that will be explained next. The corresponding time constants, τ_1 and τ_2, were 7600 s and 6.97×10^4 s, respectively.

The physical interpretation of this behavior can best be described by the Langmuir adsorption model for competing species.[40] To convert the longitudinal resistivity in Figure 2 (b) to a corresponding device carrier density in the inset, the two quantities' relationship was determined for each device and averaged, as shown in Figure 3. Since the devices were

presumed to have a significantly lower population of physical adsorbates (but not of chemically bonded $Cr(CO)_3$) due to prolonged annealing, the gas species to which the devices presumably were exposed included atmospheric dopants, namely N_2 (78.1 %), O_2 (20.9 %), and Ar (0.93 %) as well as water vapor. Other constituents are several orders of magnitude lower in concentration. Argon and nitrogen were neglected due to weak interactions with graphene compared to other constituents.[41–43] This leaves O_2, but H_2O must also be added in the appropriate amount. At 25 °C and 35 % to 40 % relative humidity, the expected percentage contribution of water vapor to the ambient environment, in terms of mass, is between 0.8 % and 0.9 %. The time-dependent function for the occupancy of one of two competing gaseous species (in this case, oxygen) is:[43]

$$\frac{d\theta_{O_2}}{dt} = k_{O_2,A} p_{O_2}\left(1 - \theta_{O_2}(t) - \theta_{H_2O}(t)\right) - k_{O_2,D}\theta_{O_2}(t) \quad (2)$$

$\theta_{O_2}(t)$ and $\theta_{H_2O}(t)$ are the fractional occupancies of oxygen and water on EG's available surface sites. The quantities k_{o_2} and p_{o_2} are the rate constants (A for adsorption and D for desorption) and unitless ratio of oxygen's partial pressure to the total pressure. For the differential equation involving $\theta_{H_2O}(t)$, the two molecule subscripts need to be swapped.

From these coupled first-order ordinary differential equations, one can determine both the final occupancy percentage for each species at equilibrium as well as the form taken by $\theta_{gas}(t)$, which includes two exponential decay terms. The final predicted occupancies of oxygen and water are approximately 90 % and 10 %, respectively. More mathematical details are provided in the Supplementary Data.

When the carrier density is fit to the two decay terms from the Langmuir model, the time constants listed earlier provide an optimized reduced chi-squared. Previously reported work indicates that adsorption of oxygen and water on graphene takes place on a similar order of magnitude,[44–48] with oxygen adsorption taking place at slightly slower times at room temperature, assuming that the adsorption follows an Arrhenius behavior. A more detailed analysis of the time-dependency of water adsorption revealed a τ_{H_2O}. of about 130 min,[44] which agrees quite well with our first time constant. The second constant requires more careful treatment to justify. With both species of gases occupying roughly equal areas for times below 2 hr, water must undergo significant desorption to accommodate for the equilibrium occupancies. A different study on EG measured a time constant on the same order of magnitude when the device was exposed to room temperature air.[49] We can make an estimation based on the measured water desorption energy of 360 meV,[48] and by use of the formula $k_A = v\exp\left[\frac{-E_{\text{ads}}}{k_B T}\right]$, where E_{ads} is the adsorption energy per molecule, v is an attempt frequency (in this case, the attempt frequency is the vibrational frequency of the molecule, usually approximated as 10^{13} s^{-1}), k_B is the Boltzmann constant, and T is temperature (K), the estimated time constant is on the order of 10^6 s, which is about 15

times higher than our fit value. Inaccuracies can arise from two factors: (1) the uncertainty of the desorption energy on EG, which can contribute an order-of-magnitude change to the time constant, and (2) the significant increase of hydrophobicity found in EG versus other forms of graphene, which would cause desorption to occur on faster time scales.[47]

4.2 Quantifying the IHE and Determining Long-Term Stability of the Carrier Density

The amount of IHE (shown as x_i in Figure 2) was quantified in Equation 1 and used to shift the carrier density by a desired amount. This correlation is shown in Figure 3 (a). The two data point colors indicate two different types of devices since some devices were older by a year compared with the newer devices. The data in pink come from devices mounted on a 12-pin package, whereas the data in green were acquired with devices mounted on a 32-pin package and allowed for more regions of the millimeter-scale EG to be tested. The error bars correspond to the uncertainties generated by the variation across the device, only present in the 32-pin package since the 12-pin package was only used to monitor one region's carrier density. There is a clear linear trend within the order of magnitude of carrier density that is most suitable for resistance metrology. Figure 3 (b), as described earlier, is a plot of the relationship between the longitudinal resistivity and carrier density, both measured at 1.6 K using the length of the device as 640 μm and the width as 400 μm for the conversion from a measured resistance. From this plot, we are also able to determine the mobilities of the device regions which span two orders of magnitude, from 10^4 $cm^2V^{-1}s^{-1}$ to 10^5 $cm^2V^{-1}s^{-1}$.

Now that the tunability and reversibility of functionalized EG have been explored, the issue of long term stability remains. Figure 3 (c) shows an example device stored in air over the course of one year and exhibits stability such that shifts are less than 10^{11} cm^{-2}. Despite the appearance of the Hall plateau as flat at this low carrier density, precision measurements suggest that the plateau is not quantized to within parts in 10^8. Thus, some additional electrons are needed, but with this level of stability in air coupled with the linear relationship between IHE and carrier density, we can develop resistance standards that have a shelf life longer than one year.

4.3 Tuning EG Devices for Metrological Applications

With the knowledge that devices exposed to air retain a stable, but low, carrier density (less than 10^{11} cm^{-2}), and the method to apply a specific amount integrated heat, we are now able to tune devices to a carrier density which enables metrological access to the quantum Hall effect.[11] Device quantization was verified by measuring the longitudinal resistivity $\rho_{xx} = V_{xx}/I_{SD} * w/l$ where V_{xx} is the voltage drop across the potential contacts, I_{SD} is the source/drain current and w and l are the width of the Hall bar and the distance between the potential contacts, respectively. If ρ_{xx} becomes negligibly small, the Hall resistance R_H becomes quantized, for example, at the $\nu = 2$ plateau with $R_H = V_{xy}/I_{SD} = R_k/2$, where R_k is the von Klitzing constant. Thus, clear indication of a breakdown of resistance quantization can be identified through changes in the resistivity that depend on the magnetic flux density, temperature, and current.[50]

Figure 4 shows resistivity measurements of an EG device of dimensions 1.6 mm × 0.4 mm (Fig. 4 (a)) that were collected using a nanovoltmeter and a ramping voltage source that are

both normally used in a two-terminal cryogenic current comparator bridge for high resistance measurements.[51] The voltage source was operated at voltages of ±0.5 V, ±1.1 V and ±5 V, allowing for currents up to about 387 μA in the $\nu = 2$ quantum Hall regime. Increasing the temperature from 1.5 K to 4 K at a high current of 387 μA had no measurable impact on the longitudinal resistivity at magnetic flux densities greater than 6 T (Fig. 4 (b), upper panels) and reducing the current only increased measurement noise (Fig. 4 (b), lower panels). In all measurements, an offset of about $\rho_{XX} = 0.25\ \text{m}\Omega$ (about $10^{-8}\ R_\text{K}$) was observed, likely to be the result of circuit leakage or nanovoltmeter input leakage in the measurement, since similar offsets were also observed using many functionalized and untreated samples. However, since there is no temperature or current dependent behavior over a wide range of magnetic flux densities, in agreement with the guidelines for reliable dc measurements of the QHR, we expect the devices to be well quantized despite the small offset.

5. CONCLUSION

Chemically functionalized EG has been shown to maintain a low and stable carrier density for at least one year, allowing it to be a promising candidate for the development of QHR standards with a long shelf life. The major difficulty of stabilizing the carrier density under ambient conditions has been solved with $Cr(CO)_3$ to the point where devices retain metrological usefulness, even after long-term storage and many temperature cycles between 1.5 K to 360 K, by a reversible and easily controllable tuning process. Through precision measurements, we have shown that hexahapto functionalization is suitable for exceptionally robust QHR standards operating at 4 K and 7 T, with applied measurement voltages up to 5 V. Overall, these results show progress toward EG sensors and electronic devices that can achieve long useful lifetimes and predictable characteristics in ambient conditions.

Supplementary Material

Refer to Web version on PubMed Central for supplementary material.

ACKNOWLEDGMENT

A.F.R and H.M.H would like to thank the National Research Council's Research Associateship Program for the opportunity. The work of B.-Y.W. at NIST was made possible by arrangement with Prof. C.-T. Liang of National Taiwan University. P.E.J. would like to thank NIST for the Summer High School Intern Program (SHIP) opportunity. S.Z. would like to thank Theiss Research for the opportunity.

Funding Sources

All work performed as part of the duties of employees of the United States Government, along with its associated and guest researchers.

REFERENCES

[1]. Geim AK, Novoselov KS. The rise of graphene. Nat. Mater, 6 (2007), pp. 183–191. [PubMed: 17330084]

[2]. Novoselov KS, Geim AK, Morozov SV, Jiang D, Zhang Y, Dubonos SV, et al. Electric field effect in atomically thin carbon films. Science, 306 (2004), pp. 666–669. [PubMed: 15499015]

[3]. Novoselov KS, Fal'ko VI, Colombo L, Gellert PR, Schwab MG, Kim K. A roadmap for graphene. Nature, 490 (2012), pp. 192–200. [PubMed: 23060189]

[4]. Kruskopf M and Elmquist RE. Epitaxial graphene for quantum resistance metrology. Metrologia, 55 (2018), pp. R27–R36.

[5]. Janssen TJBM, Tzalenchuk A, Yakimova R, Kubatkin S, Lara-Avila S, Kopylov S, et al. Anomalously strong pinning of the filling factor nu = 2 in epitaxial graphene. Phys Rev B, 83 (2011), pp. 233402–1–233402–4.

[6]. Ribeiro-Palau R, Lafont F, Brun-Picard J, Kazazis D, Michon A, Cheynis F, et al. Quantum Hall resistance standard in graphene devices under relaxed experimental conditions. Nature Nanotechnol, 10 (2015), pp. 965–971. [PubMed: 26344181]

[7]. Tzalenchuk A, Lara-Avila S, Kalaboukhov A, Paolillo S, Syväjärvi M, Yakimova R, et al. Towards a quantum resistance standard based on epitaxial graphene. Nat Nanotechnol, 5 (2010), pp. 186–189. [PubMed: 20081845]

[8]. Real MA, Shen T, Jones GR, Elmquist RE, Soons JA, Davydov AV. Graphene epitaxial growth on SiC(0001) for resistance standards. IEEE Trans. Instrum. Meas, 62 (2013), pp. 1454–1460.

[9]. Lafont F, Ribeiro-Palau R, Kazazis D, Michon A, Couturaud O, Consejo C, et al. Quantum Hall resistance standards from graphene grown by chemical vapour deposition on silicon carbide. Nat. Comm, 6 (2015), p. 6806–1–6806–9.

[10]. Janssen TJBM, Rozhko S, Antonov I, Tzalenchuk A, Williams JM, Melhem Z, et al. Operation of graphene quantum Hall resistance standard in a cryogen-free table-top system. 2D Mater., 2 (2015), pp. 035015–1–035015–9.

[11]. Jeckelmann B, Jeanneret B. The quantum Hall effect as an electrical resistance standard. Rep. Prog. Phys, 64 (2001), pp. 1603–1655.

[12]. Lara-Avila S, Moth-Poulsen K, Yakimova R, Bjørnholm T, Fal'ko V, Tzalenchuk A, et al. Non-volatile photochemical gating of an epitaxial graphene/polymer heterostructure. Adv Mater, 23 (2011), pp. 878–882. [PubMed: 21328484]

[13]. Yang Y. Cheng G, Mende P, Calizo IG, Feenstra RM, Chuang C, et al. Epitaxial Graphene Homogeneity and Quantum Hall Effect in Millimeter-Scale Devices. Carbon, 115 (2017), pp. 229–236. [PubMed: 28924301]

[14]. Novikov S, Lebedeva N, Pierz K, Satrapinski A. Fabrication and Study of Large-Area QHE Devices Based on Epitaxial Graphene. IEEE Trans. Instrum. Meas, 64 (2015), pp. 1533–1538.

[15]. He H, Kim KH, Danilov A, Montemurro D, Yu L, Park YW, et al. Uniform doping of graphene close to the Dirac point by polymer-assisted spontaneous assembly of molecular dopants. Nat. Commun, 9 (2018), pp. 3956–1–3956–7. [PubMed: 30262825]

[16]. Hollander MJ, LaBella M, Hughes ZR, Zhu M, Trumbull KA, Cavalero R, et al. Enhanced transport and transistor performance with oxide seeded high-κ gate dielectrics on wafer-scale epitaxial graphene. Nano Lett, 11 (2011), pp. 3601–3607. [PubMed: 21805989]

[17]. Robinson JA, LaBella M, Trumbull KA, Weng XJ, Cavelero R, Daniels T, et al. Epitaxial graphene materials integration: effects of dielectric overlayers on structural and electronic properties. ACS Nano, 4 (2010), pp. 2667–2672. [PubMed: 20415460]

[18]. Alaboson JMP, Wang QH, Emery JD, Lipson AL, Bedzyk MJ, Elam JW, et al. Seeding atomic layer deposition of high-k dielectrics on epitaxial graphene with organic self-assembled monolayers. ACS Nano, 5 (2011), pp. 5223–5232. [PubMed: 21553842]

[19]. Garces NY, Wheeler VD, Hite JK, Jernigan GG, Tedesco JL, Nepal N, et al. Epitaxial graphene surface preparation for atomic layer deposition of Al(2)O(3). J Appl Phys, 109 (2011), pp. 124303–1–124303–6.

[20]. Rigosi AF, Liu C-I, Wu B-Y, Lee H-Y, Kruskopf M, Yang Y, et al. Examining epitaxial graphene surface conductivity and quantum Hall device stability with Parylene passivation. Microelectronic Eng., 194 (2018), pp. 51–55.

[21]. Rigosi AF, Liu C-I, Wu B-Y, Lee H-Y, Kruskopf M, Yang Y, et al. Quantum Hall Device Data Monitoring Following Encapsulating Polymer Deposition. Data in Brief, 20 (2018), pp. 1201–1208. [PubMed: 30238028]

[22]. Rigosi AF, Liu C-I, Glavin NR, Yang Y, Hill HM, Hu J, et al. Electrical Stabilization of Surface Resistivity in Epitaxial Graphene Systems by Amorphous Boron Nitride Encapsulation. ACS Omega, 2 (2017), pp. 2326–2332. [PubMed: 28828410]

[23]. Rigosi AF, Glavin NR, Liu C-I, Yang Y, Obrzut J, Hill HM, et al. Preservation of Surface Conductivity and Dielectric Loss Tangent in Large-Scale, Encapsulated Epitaxial Graphene Measured by Noncontact Microwave Cavity Perturbations. Small, 13, (2017), 1700452–1–1700452–7.

[24]. Bresnehan MS, Hollander MJ, Wetherington M, Labella M, Trumbull KA, Cavalero R, et al. Integration of hexagonal boron nitride with quasi-freestanding epitaxial graphene: toward wafer-scale, high-performance devices. ACS Nano, 6 (2012), pp. 5234–5241. [PubMed: 22545808]

[25]. Hu J, Rigosi AF, Kruskopf M, Yang Y, Wu B-Y, Tian J, et al. Towards epitaxial graphene p-n junctions as electrically programmable quantum resistance standards. Sci. Rep, 8 (2018), pp. 15018–1–15018–11. [PubMed: 30301948]

[26]. Yang Y, Huang L-I, Fukuyama Y, Liu HF, Real MA, Barbara P, et al. Low Carrier Density Epitaxial Graphene Devices on SiC. Small, 11 (2015), pp. 90–95. [PubMed: 25136792]

[27]. Wehling TO, Novoselov KS, Morozov SV, Vdovin EE, Katsnelson MI, Geim AK, et al. Molecular doping of graphene. Nano Letters, 8 (2008), pp. 173–177. [PubMed: 18085811]

[28]. Ni ZH, Wang HM ZQ, Luo ZQ, Wang YY, Yu T, Wu YH, et al. The effect of vacuum annealing on graphene. J Raman Spectroscopy, 41 (2009), pp. 479–483.

[29]. Nomani MWK, Shields V, Tompa G, Sbrockey N, Spencer MG, Webb RA, et al. Correlated conductivity and work function changes in epitaxial graphene. Appl Phys Lett, 100 (2012), pp. 092113–1–092113–4.

[30]. Kruskopf M, Pakdehi DM, Pierz K, Wundrack S, Stosch R, Dziomba T, et al. Comeback of epitaxial graphene for electronics: large-area growth of bilayer-free graphene on SiC. 2D Mater., 3 (2016), pp. 041002–1–041002–9.

[31]. Panchal V, Yang Y, Cheng G, Hu J, Liu C-I, Rigosi AF, et al. Rapid characterization of wafer-scale epitaxial graphene and graphene nanoribbons on SiC. arXiv:1711.03563 (2017), pp. 1–30.

[32]. Sarkar S, Niyogi S, Bekyarova E, and Haddon RC. Organometallic chemistry of extended periodic pi-electron systems: hexahapto-chromium complexes of graphene and single-walled carbon nanotubes. Chem. Sci, 2 (2011), pp. 1326–1333.

[33]. Bekyarova E, Sarkar S, Niyogi S, Itkis ME, and Haddon RC. Advances in the chemical modification of epitaxial graphene. J. Phys. D: Appl. Phys, 45 (2012), pp. 154009–1–154009–18.

[34]. Sarkar S, Zhang H, Huang J-W, Wang F, Bekyarova E, Lau CN, et al. Organometallic hexahapto functionalization of single layer graphene as a route to high mobility graphene devices. Adv. Mater, 25 (2013), pp. 1131–1136. [PubMed: 23136073]

[35]. Dai J, Zhao Y, Wu X, Zeng XC, and Yang J. Organometallic Hexahapto-Functionalized Graphene: Band Gap Engineering with Minute Distortion to the Planar Structure. J. Phys. Chem. C, 117 (2013), pp. 22156–22161.

[36]. Che S, Jasuja K, Behura SK, Nguyen P, Sreeprasad TS, and Berry V. Retained Carrier-Mobility and Enhanced Plasmonic-Photovoltaics of Graphene via ring-centered η6 Functionalization and Nanointerfacing. Nano Lett, 17 (2017), pp. 4381–4389. [PubMed: 28586228]

[37]. Chen M, Pekker A, Li W, Itkis ME, Haddon RC, and Bekyarova E. Organometallic chemistry of graphene: Photochemical complexation of graphene with group 6 transition metals. Carbon, 129 (2018) pp. 450–455.

[38]. Wright KD and Barron AR. Catalyst Residue and Oxygen Species Inhibition of the Formation of Hexahapto-Metal Complexes of Group 6 Metals on Single-Walled Carbon Nanotubes. J. Carbon Res, 3 (2017), pp. 17–1–17–15.

[39]. Biesinger MC, Payne BP, Grosvenor AP, Lau LWM, Gerson AR, and Smart RSC. Resolving surface chemical states in XPS analysis of first row transition metals, oxides and hydroxides: Cr, Mn, Fe, Co and Ni. Appl. Surf. Sci, 257 (2011), pp. 2717–2730.

[40]. Maier K, Helwig A, Muller G, Hille P, Teubert J, Eickhoff M, Competitive adsorption of air constituents as observed on InGaN/GaN nano-optical probes. Sens. Actuator B, 250 (2017), pp. 91–99.

[41]. Farmer DB, Perebeinos V, Lin Y-M, Dimitrakopoulos C, and Avouris P, Charge trapping and scattering in epitaxial graphene. Phys. Rev. B, 84 (2011), pp. 205417–1–205417–5.

[42]. Pinto H and Markevich A, Electronic and electrochemical doping of graphene by surface adsorbates. Beilstein J. Nanotechnol, 5 (2014), pp. 1842–1848. [PubMed: 25383296]

[43]. Chuang C, Yang Y, Pookpanratana S, Hacker CA, Liang C-T, and Elmquist RE, Chemical-doping-driven crossover from graphene to “ordinary metal” in epitaxial graphene grown on SiC. Nanoscale, 9 (2017), pp. 11537–11544. [PubMed: 28767112]

[44]. Yavari F, Kritzinger C, Gaire C, Song L, Gullapalli H, Borca-Tasciuc T, et al. Tunable Bandgap in Graphene by the Controlled Adsorption of Water Molecules. Small, 6 (2010), pp. 2535–2538. [PubMed: 20963796]

[45]. Silvestre I, de Morais EA, Melo AO, Campos LC, Goncalves A-MB, Cadore AR, et al., Asymmetric Effect of Oxygen Adsorption on Electron and Hole Mobilities in Bilayer Graphene: Long- and Short-Range Scattering Mechanisms. ACS Nano, 7 (2013), pp. 6597–6604. [PubMed: 23859671]

[46]. Bagsican FR, Winchester A, Ghosh S, Zhang X, Ma L, Wang M, et al., Adsorption energy of oxygen molecules on graphene and two-dimensional tungsten disulfide. Sci. Rep, 7 (2017), pp. 1774–1–1774–10. [PubMed: 28496178]

[47]. Melios C, Giusca CE, Panchal V, and Kazakova O, Water on graphene: review of recent progress. 2D Mater., 5 (2018), pp. 022001–1–022001–18.

[48]. Bottcher S, Vita H, Weser M, Bisti F, Dedkov YS, and Horn K, Adsorption of Water and Ammonia on Graphene: Evidence for Chemisorption from X−ray Absorption Spectra. J. Phys. Chem. Lett, 8 (2017), pp. 3668–3672. [PubMed: 28732444]

[49]. Panchal V, Giusca CE, Lartsev A, Martin NA, Cassidy N, Myers-Ward RL, et al., Atmospheric doping effects in epitaxial graphene: correlation of local and global electrical studies. 2D Mater., 3 (2016), pp. 015006–1–015006–10.

[50]. Delahaye F, Jeckelmann B, Revised technical guidelines for reliable dc measurements of the quantized Hall resistance. Metrologia 5, 40 (2013), pp. 217–218.

[51]. Hernandez-Marquez FL, Bierzychudek ME, Jones GR, and Elmquist RE, Precision high-value resistance scaling with a two-terminal cryogenic current comparator, Rev. Sci. Instrum, 85 (2014), pp. 044701–1–044701–6. [PubMed: 24784632]

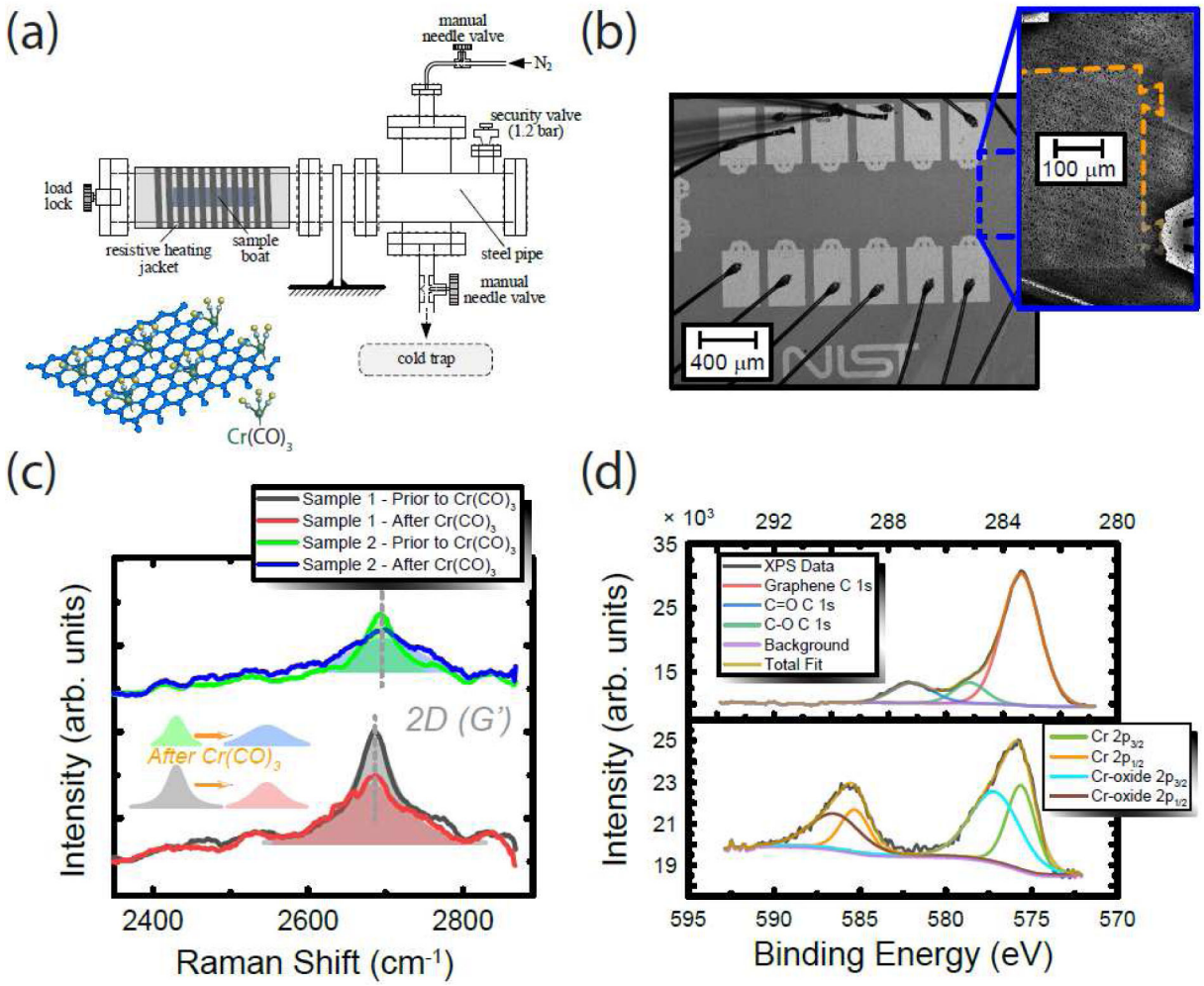

Figure 1.

(a) Drawing of the furnace for functionalization processes and rendering of the graphene crystal structure functionalized with $Cr(CO)_3$. (b) An image of one device, taken at 5 × and 20 × (inset) magnification with a confocal laser scanning microscope, after functionalization. The inset uses a fading orange dashed line to mark the EG edge. Black dots appear on the surface which are clusters of CrO_3, as described by XPS measurements. (c) Raman spectra for two devices, taken both before (green and black curves and areas) and after (blue and red curves and areas) functionalization. (d) XPS spectra for the surface presence of carbon (C 1s) and chromium (Cr 2p) in the top and bottom panel, respectively.

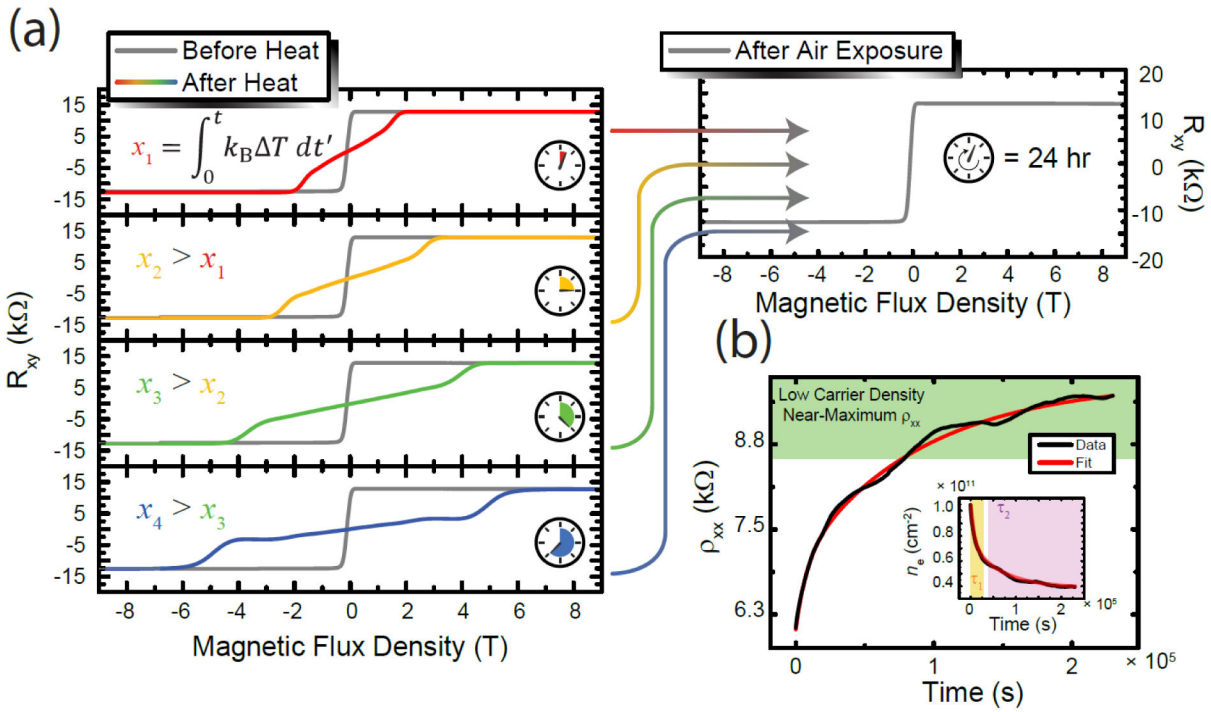

Figure 2.

(a) The Hall resistance for some devices are shown at 1.6 K, with all gray curves representing data after the device has been left to stabilize in air for 24 h or more, before temperatures above 300 K were applied. Each of the four panels depicts a different measurement where the device was first allowed to chemically equilibrate with air, followed by annealing in vacuum. The total IHE increases with each panel. In all cases, when the device is left in air for a period of at least one day, the device's carrier density returns to a value on the order of 10^{10} cm^{-2}. (b) When the device is warmed up to room temperature and stored in air, the longitudinal resistivity shifts and asymptotically reaches a maximum over approximately 70 hr, resulting in a Fermi level of EG that is close to the Dirac point. Two exponential decays comprise this behavior, as seen in the inset, and are then used to fit the data.

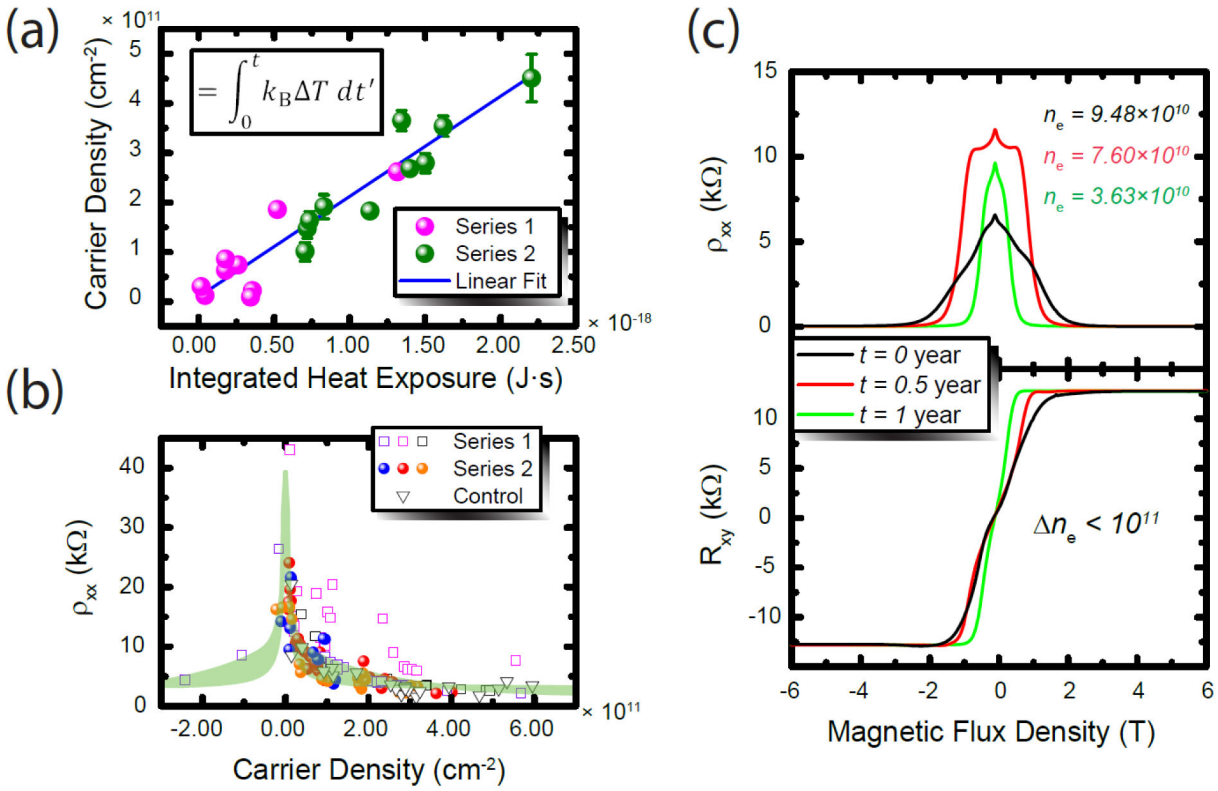

Figure 3.

(a) The correlation between integrated heat exposure and the subsequently-measured carrier density at 1.6 K is shown, with different color data points representing different packages onto which devices were mounted, with Series 1 (pink) and 2 (green) corresponding to the 12-pin and 32-pin packages, respectively. Error bars represent 1σ uncertainties of the average of multiple measurable regions on the device. (b) The relationship between carrier density and longitudinal resistivity, both measured at 1.6 K. (c) The stability of the carrier density is demonstrated to be less than 10^{11} cm^{-2} for the same device exposed to air over the course of one year. This is an indication that $Cr(CO)_3$ has remained on the EG surface and could be a suitable material for metrological applications.

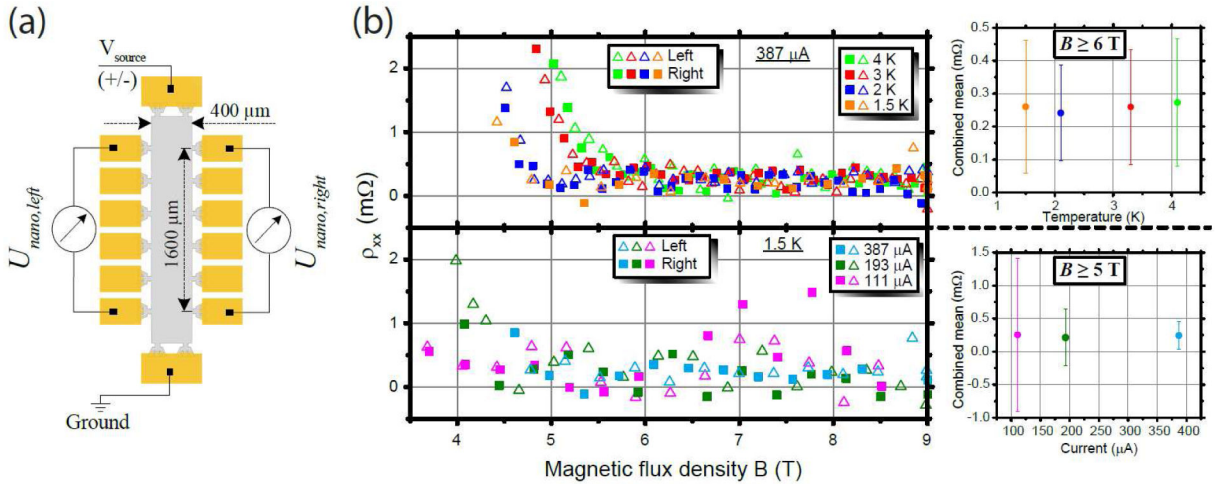

Figure 4.

Resistivity measurements in the QHE regime at the low potential side of the Hall bar. (a) The measurement configuration of the graphene QHR device (1600 µm x 400 µm) for the determination of the resistivity along the right and the left side of the device with polarity reversal. (b) The vanishing of the resistivity on both sides of the Hall bar at high fields indicates resistance quantization at a current of 387 µA and temperatures up to 4 K (upper diagram). Increasing the current from 111 µA to 387 µA at 1.5 K (lower diagram) results in reduced noise but is not corelated with an increase in the resistivity. Also shown are the scatterplots of the corresponding resistivity measurements for increasing temperatures (upper) and increasing currents (lower) summarize the results by taking the mean value of the left and the right side of the Hall bar for $B \geq 6$ T and $B \geq 5$ T. Error bars represent 1σ uncertainties of the average of all color-coded measurements above the indicated magnetic flux density.